# $Bi_{1-x}Ca_xMnO_3$ ($x$ = 0.4 and 0.45): X-ray Single-Crystal and Electron Microscopy Study

M. Giot,[†,‡] P. Beran,[†] O. Pérez,*,[†] S. Malo,[†] M. Hervieu,[†] B. Raveau,[†] M. Nevriva,[§]
K. Knizek,[‖] and P. Roussel[⊥]

*Laboratoire CRISMAT, UMR 6508 CNRS ENSICAEN, 6 bd Maréchal Juin, 14050 Caen Cedex 4, France,
Laboratoire Léon Brillouin, CEA/Saclay, 91191 Gif-sur-Yvette Cedex, France, Institute of Chemical
Technology in Prague, Technicka 5, 16628 Praha 6, Czech Republic, Institute of Physics, Cukrovarnicka
10, 16253 Prague 6, Czech Republic, and Laboratoire de Cristallochimie et Physicochimie du Solide,
UMR CNRS 8012, Université des Sciences et Technologies de Lille, B.P. 108,
59652 Villeneuve d'Ascq Cedex, France*

The superstructure of $Bi_{1-x}Ca_xMnO_3$ ($x$ = 0.4 or 0.45), which exhibits a charge/orbital-ordered state at room temperature ($T_{CO} \approx$ 330 K), has been successfully determined at different temperatures using single-crystal X-ray diffraction data and the superspace formalism. This peculiar approach provides a very convenient way to analyze all possible 3D symmetry ($P2_1/m$, $Pm$, and $Pnm2_1$) of the superstructure. The structural model of the ordered state has been confirmed thanks to complementary data from several other techniques (electron diffraction, high-resolution electron microscopy (HREM), and synchrotron high-resolution X-ray powder diffraction, all vs $T$). It is compatible with an orthorhombic cell ($a$ = 11.002(2) Å, $b$ = 7.588(1) Å, $c$ = 5.425(4) Å at 150 K) and the space group $Pnm2_1$. The structural model is based on the alternation of one double band of $Mn(1)O_6$ octahedra and one double band of $Mn(2)O_6$ octahedra, the two octahedron types exhibiting almost similar distortion. HREM images were then simulated from the refined atomic positions; the good agreement with the experimental images confirms the model. Finally, the relationships between structural characterizations and magnetic properties have been investigated for these compounds.

## Introduction

Charge ordering (CO) is one of the most fascinating but controversial phenomena that have been studied to date in manganites since the discovery of colossal magnetoresistance in these compounds. First established in the $La_{1-x}Ca_xMnO_3$ series[1,2] with $x \approx 0.5$ as a 1:1 ordering of $Mn^{3+}$ and $Mn^{4+}$ species, this effect has been more recently discussed in different $Ln_{0.5}Ca_{0.5}MnO_3$ manganites (Ln = lanthanide).[3−6] Charge ordering is associated with orbital ordering (OO) due to the cooperative Jahn−Teller distortion that exists for $Mn^{3+}$ and which is detectable by structural studies. Thus, the magnetic and transport transitions observed in the $Ln_{0.5}Ca_{0.5}MnO_3$ manganites are often interpreted as the combined influence of CO and OO.[7−8] The analysis of the $MnO_6$ octahedron distortion (i.e., the Mn−O distances and O−Mn−O

angles) and average Mn−O distances provides information about the electronic state of each Mn site. Unfortunately, the majority of structural investigations is performed on powder manganite samples, so the results are subject to controversy due to pseudosymmetry effects. Moreover, the intrinsic twinning of the crystals makes the structural refinements tricky.[3,8−10] and it is difficult to prepare large single crystals of half-doped manganites for neutron diffraction studies.

However, in a recent accurate single-crystal study of $Pr_{0.6}Ca_{0.4}MnO_3$, Daoud-Aladine et al. concluded that the standard CO/OO model is not valid, but that the transition at $T_{CO}$ corresponds to a so-called Zener polaron order, the atomic positions suggesting the trapping of electrons within pairs of Mn, involving a local double-exchange phenomenon and a polaronic-like distortion.[11] For this $Pr_{0.6}Ca_{0.4}MnO_3$ manganite, the standard CO/OO model[8] considers the $P2_1/m$

* To whom correspondence should be addressed. E-mail: olivier.perez@
ensicaen.fr. Phone: 33 (0)2 31 45 26 13. Fax: 33(0)2 31 95 16 00.
  † UMR 6508 CNRS ENSICAEN.
  ‡ CEA/Saclay.
  § Institute of Chemical Technology in Prague.
  ‖ Institute of Physics.
  ⊥ Laboratoire de Cristallochimie et Physicochimie du Solide.

(1) Goodenough, J. B. *Phys. Rev.* **1955,** *100,* 564.
(2) Wollan, E. O.; Koehler, W. C. *Phys. Rev.* **1955,** *100,* 545.
(3) Woodward, P. M.; Cox, D. E.; Vogt, T.; Rao, C. N. R.; Cheetham, A. K. *Chem. Mater.* **1999,** *11,* 3528.
(4) Chen, C. H.; Cheong, S. W. *Phys. Rev. Lett.* **1996,** *76,* 4042.
(5) Jirak, Z.; Krupicka, S.; Simsa, Z.; Dlouha, M.; Vratislav, S. *J. Magn. Magn. Mater.* **1985,** *53,* 153.
(6) Hervieu, M.; Barnabé, A.; Martin, C.; Maignan, A.; Damay, F.; Raveau, B. *J. Eur. Phys. B* **1999,** *8,* 31; *J. Mater. Chem.* **1998,** *8,* 1405.
(7) Chen, C. H.; Mori, S.; Cheong, S.-W. *Phys. Rev. Lett.* **1999,** *83,* 4792−4795.
(8) Radaelli, P. G.; Cox, D. E.; Marezio, M.; Cheong, S. W. *Phys. Rev. B* **1997,** *55,* 3015.
(9) Richard, O.; Schuddinck, W.; Van Tendeloo, G.; Millange, F.; Hervieu, M.; Caignaert, V.; Raveau, B. *Acta Crystallogr., A* **1999,** *55,* 704.
(10) Jirak, Z.; Damay, F.; Hervieu, M.; Martin, C.; Raveau, B.; Bourée, F. *Phys. Rev. B* **2000,** *61,* 1181.
(11) Daoud-Aladine, A.; Rodriguez-Carjaval, J.; Pinsart-Gaudart, L.; Fernandez-Diaz, M. T.; Revcolevschi, A. *Phys. Rev. Lett.* **2002,** *89,* 097205. Daoud-Aladine, A.; Rodriguez-Carjaval, J.; Pinsart-Gaudart, L.; Fernandez-Diaz, M. T.; Revcolevschi, A. *Appl. Phys. A* **2002,** *74,* S1758. Daoud-Aladine, A. Ph.D. Thesis, Laboratoire Léon Brillouin, France, 2001.

space group (SG) while the Zener polaron model[11] is described with the $Pnm2_1$ SG (as approximate for $P1m1$), both SGs belonging to the possible isotropy subgroups of $Pnma$, which is that observed above $T_{CO}$. Let us note that $P12_1/m1$ and $Pnm2_1$ are supergroups of $P1m1$. The symmetry of the structural model of ordering in manganites is currently still being debated. Recently, a study[12] was performed with time-of-flight neutron diffraction on a high-resolution powder diffractometer at ISIS and with synchrotron high-resolution powder diffraction (SHRPD) on diffractometer ID31 at ESRF. The authors proposed indeed that the $2a_p\sqrt{2} \times 2a_p \times a_p\sqrt{2}$ supercell observed below $T_{CO}$ for $Pr_{0.5}Ca_{0.5}MnO_3$ has a $P12_1/m1$ SG and that this compound is compatible with the "$P2_1/m$ model", corresponding to Goodenough's original striped CO picture.[1]

Bearing in mind the above considerations, the studies carried out on $Bi_{1-x}Sr_xMnO_3$[13-16] and $Bi_{1-x}Ca_xMnO_3$[17-21] systems are of great interest. For $x = 0.5$ these compounds exhibit indeed a resistive transition, attributed to the CO/OO effect, with high values of $T_{CO}$, ~475 K for $Bi_{0.5}Sr_{0.5}MnO_3$[13] and ~325 K for $Bi_{0.5}Ca_{0.5}MnO_3$.[17-19] However, due to the lack of single crystals, no precise information has been reported about the nature of charge and orbital ordering. Nevertheless, thanks to their high $T_{CO}$, these systems provide the opportunity to characterize this ordered state at room temperature by combining X-ray diffraction and high-resolution electron microscopy (HREM) data. As previously reported for $Bi_{0.5}Sr_{0.5}MnO_3$,[16] HREM supplies images which cannot be interpreted assuming the model of the simple alternation of $Mn^{3+}$ and $Mn^{4+}$ octahedra. We have prepared single crystals for revisiting in that viewpoint the systems Bi–Ca–Mn–O and Bi–Sr–Mn–O. The crystals obtained in the Ca-based system are small ($V \leq 0.1 \times 0.1 \times 0.1$ mm³), but the majority of the selected ones have the advantage of being almost free of twinning (see further), allowing then an accurate X-ray diffraction (XRD) study. In the present paper, we report in detail the structural properties of a $Bi_{0.6}Ca_{0.4}MnO_3$ single crystal. The results obtained by single-crystal XRD have been completed by crushing the analyzed crystal for electron microscopy study and by SHRPD measurements in connection with the physical properties. They are last compared with those obtained for $Bi_{0.55}Ca_{0.45}MnO_3$, leading to a unique picture for the description of the low-temperature state. The model refined from single-crystal

(12) Goff, R. J.; Attfield, P. *Phys. Rev. B* **2004**, *70*, 140404.
(13) Garcia-Munoz, J. L.; Frontera, C.; Aranda, M.; Llobet, A.; Ritter, C. *Phys. Rev. B* **2001**, *63*, 64415.
(14) Schiffer, P.; Ramirez, A. P.; Bao, W.; Cheong, S. W. *Phys. Rev. Lett.* **1995**, *75*, 3336.
(15) Frontera, C.; García-Muñoz, J. L.; Aranda, M.; Hervieu, M.; Ritter, C.; Mañosa, L. *Phys. Rev. B* **2003**, *68*, 134408.
(16) Hervieu, M.; Maignan, A.; Martin, C.; Nguyen, N.; Raveau, B. *Chem. Mater.* **2001**, *13*, 1356.
(17) Frontera, C.; Garcia-Munoz, J. L.; Aranda, M.; Ritter, C.; Llobet, A.; M. Respaud Vanacken, J. *Phys. Rev. B* **2001**, *64*, 54401.
(18) Bokov, V. A.; Grogoryan, N. A.; Bryzhina, M. F. *Phys. Status Solidi* **1967**, *20*, 745.
(19) Woo, H.; Tyson, T. A.; Croft, M.; Cheong, S.-W.; Woicik, J. C. *Phys. Rev. B* **2001**, *63*, 134412.
(20) Chiba, H.; Kikushi, M.; Kusaba, K.; Muraoka, Y.; Syono, Y. *Solid State Commun.* **1996**, *99*, 499.
(21) Hervieu, M.; Malo, S.; Perez, O.; Beràn, P.; Martin, C.; Baldinozzi, G.; Raveau, B. *Chem. Mater.* **2003**, *15*, 523.

X-ray data explains the high-resolution electron microscopy contrast.

## Crystal Growth

Crystals were grown by the flux technique, using $Bi_2O_3$ as a flux, to avoid contamination. For the two batches, the precursors $Bi_2O_3$, $CaMnO_3$ (prepared in air at 800 °C, starting from $CaCO_3$ and $MnCO_3$), and $MnO_2$ were mixed in an agate mortar in stoichiometric ratios Bi:Ca:Mn = 60:40:100 and Bi:Ca:Mn = 55:45:100. A $Bi_2O_3$ excess (82.5% in weight) was added, placed in a 35 cm³ platinum crucible, and preheated at 700 °C for 12 h. For this mixture, the eutectic and liquidus temperatures were determined at $T_E$ = 720 °C and $T_L$ = 1044 °C, respectively. The growth was carried out by increasing the temperature up to $T_L$ + 50 °C, with a rate of 100 °C/h. After a soaking time at this temperature of 12 h, the mixture was cooled to room temperature with a rate of 4 °C/h. The crystals isolated from the bulk by heating the mixture in a nitric acid solution had the shape of cubes with a typical dimension of 5 mm, but after a few hours, they were split in the form of small platelets. The energy-dispersive spectroscopy analyses of numerous crystallites allowed the cationic compositions "$Bi_{0.60(5)}Ca_{0.40(5)}Mn_1$" and "$Bi_{0.55(5)}Ca_{0.45(5)}Mn_1$" to be confirmed (calculated for one Mn per formula).

## Single-Crystal X-ray Diffraction

A preliminary X-ray diffraction investigation was performed on single crystals at room temperature, using Mo Kα radiation on a Kappa CCD (Bruker Nonius) diffractometer. Large $\Omega$ and $\chi$ scans were used to control the crystalline quality of different crystals and to determine the cell parameters. A single crystal of suitable size ($\cong 0.10 \times 0.10 \times 0.10$ mm³) was then selected. Frames were collected, for $0 < \theta < 30°$, with a classical strategy using $\Phi$ scans at constant $\Omega$ and $\Omega$ scans at constant $\Phi$ ($\Phi/\Omega$ scans), a small scan angle (0.3 deg/frame), and a short sample–detector distance ($D_x$ = 34 mm). The absence of splitting of the reflections evidenced that the data have been recorded for a single domain, as further confirmed during the refinement. The plots of reciprocal lattice planes assembled from these series of experimental frames are sufficiently complete and have sufficient resolution to examine the presence or absence of superlattice reflections.

$Bi_{0.6}Ca_{0.4}MnO_3$ exhibits a transition at about 330 K, as previously mentioned by Bokov et al.[18] To characterize the phase transition, X-ray diffraction experiments were performed at 373 K (above $T_{CO}$), at room temperature (rt) (just below $T_{CO}$), and at 150 K (far from $T_{CO}$) to prevent an artifact during the structural investigations. Below $T_{CO}$, two types of reflections can be identified in the diffraction patterns (see Figure 1 recorded at 150 K). The intense spots, called main reflections, are characteristic of an orthorhombic subcell with $a_p\sqrt{2} \times 2a_p \times a_p\sqrt{2}$ ($a_p$ being the parameter of the cubic perovskite cell), while the weaker ones, called satellite reflections, induce a doubling of the $a$ parameter. All the reflections are sharp. The main reflections are consistent with the $Pnma$ space group for the subcell. The whole diffraction
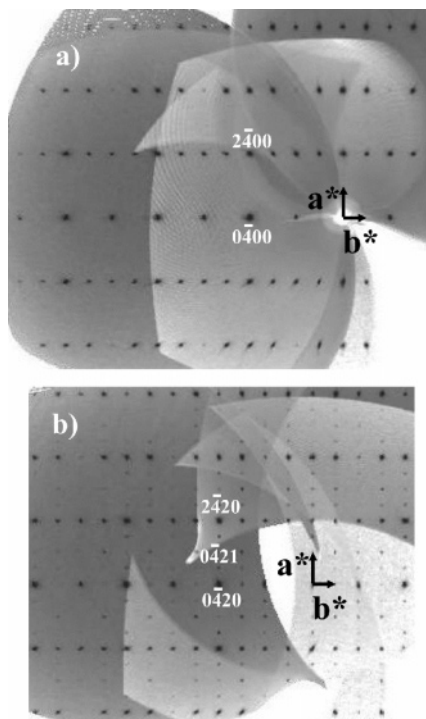
**Figure 1.** (a) ($hk0$) and (b) ($hk2$) diffraction planes calculated from low-temperature (150 K) experimental frames. Indices are given in the modulated cell $a_p\sqrt{2}$, $2a_p$, $a_p\sqrt{2}$, 90°, 90°, 90°, $\mathbf{q}^* = 1/2\mathbf{a}^*$.

pattern can be described either within a classical orthorhombic supercell approach (supercell parameters $2a_p\sqrt{2} \times 2a_p \times a_p\sqrt{2}$) or using the 4D formalism (cell parameters $a_p\sqrt{2} \times 2a_p \times a_p\sqrt{2}$ and wave vector $\mathbf{q}^* = 1/2\mathbf{a}^*$) developed for modulated structures.[22] Note that the norm of the modulation vector is invariant in the investigated range of temperatures.

In the superspace approach, a linear combination of four vectors ($\mathbf{a}^*$, $\mathbf{b}^*$, $\mathbf{c}^*$, $\mathbf{q}^*$), with integer coefficients $hklm$, are necessary to index all the reflections. The two types of peaks described above are then called $hkl0$ for the main reflections and $hklm$ with $m \neq 0$ for the satellite reflections. Note that the exact superposition of satellite reflections $hkl\bar{1}$ and ($h - 1)kl1$ clearly evidences, indeed, the commensurate character of the modulation (Figure 1b).

A suitable strategy for data collections was defined, using the precession pictures. Owing to the cell parameters and the small spot size, a scanning angle of 0.6° and a $D_x$ value of 34 mm have been chosen; $\Phi/\Omega$ scans were used. To collect a great number of weak reflections, notably the reflections corresponding to the superstructure ($hklm$, $m \neq 0$ in the 4D approach, or $hkl$, $h = 2n + 1$ in the supercell description), but avoiding any detector saturation by reflections of strong intensity, two different exposure times (240 s/deg and 24 s/deg) have been used to collect data at room temperature. For the low-temperature measurements ($T = 150$ K), an exposure time of 40 s/deg has been chosen. The diffracted intensities were collected up to $\theta = 45°$. A redundancy of 2 for 90% of the reflections was chosen. The EvalCCD software[23] was used to extract reflections from the collected frames; reflections were merged and rescaled, if

(22) De Wolff, P. M. *Acta Crystallogr., A* **1974**, *30*, 777.
(23) Duisenberg, A.; Kroon-Batenburg, L.; Shreurs, A. *J. Appl. Crystallogr.* **2003**, *36*, 220.

**Table 1. Single-Crystal X-ray Data of Bi$_{0.6}$Ca$_{0.4}$MnO$_3$**

| | $T = 373$ K | room temperature | $T = 150$ K |
|---|---|---|---|
| cell parameters | | | |
| $a$ (Å) | 5.484(5) | 10.994(7) | 11.002(2) |
| $b$ (Å) | 7.669(4) | 7.589(2) | 7.588(1) |
| $c$ (Å) | 5.403(5) | 5.430(2) | 5.425(4) |
| space group | *Pnma* | *Pnm2$_1$* | *Pnm2$_1$* |
| no. of obsd reflns ($I > 3\sigma(I)$) | 210 | 2738 | 2338 |
| $hkl$, $h = 2n$ | | 1531 | 1314 |
| $hkl$, $h = 2n + 1$ | | 1207 | 1024 |
| $(\sin \theta)/\lambda_{max}$ | 0.67 | 0.90 | 0.90 |
| internal reliability factor (%) | 5.5 | 3.8 | 6.8 |
| refinement program | Jana2000 | Jana2000 | Jana2000 |
| $R$ factor (%) | | | |
| all | 3.8 | 6.6 | 6.8 |
| $hkl$, $h = 2n$ | | 7.0 | 5.7 |
| $hkl$, $h = 2n + 1$ | | 6.1 | 10.3 |

necessary, as a function of the exposure time. Data were corrected for absorption using the Jana2000 program[24] within the analytical option based on the crystal morphology. The absorption correction is crucial in our case because of the bismuth absorption coefficient. The crystal data are gathered in Table 1.

At 150 K as at room temperature, the observed conditions limiting the possible reflections in the 4D approach ($a_p\sqrt{2}$, $2a_p$, $a_p\sqrt{2}$, 90°, 90°, 90°, $\mathbf{q}^* \approx 1/2\mathbf{a}^*$) are $0klm$, $k + l = 2n$; $hk0m$, $h = 2n$; $h00$, $h = 2n$; $0k0m$, $k = 2n$; and $00lm$, $l = 2n$, which are consistent with the superspace group $Pnma(\alpha00)00s$. Note that the intensity of the satellite reflections increases with the $l$ index; this is clearly visible both on the ($h0l$) plane and, by comparison, on the ($hk0$), ($hk1$), and ($hk2$) planes (Figure 1a). This effect results from the transverse nature of the modulation: the main atomic displacements are thus expected along the $\vec{c}$ direction. Considering the superspace group $Pnma(\alpha00)00s$, the analysis of the possible 3D sections of the supercrystal leads to the following space groups: $Pnm2_1$, $P12_1/m1$, and $P1m1$ for the supercell ($2a_p\sqrt{2}$, $2a_p$, $a_p\sqrt{2}$, 90°, 90°, 90°).

Finally, a data set was collected at 373 K, above $T_{CO} \approx 330$ K, as determined by the physical properties and electron microscopy (see the following), on a three-circle Bruker AXS SMART CCD 1K with a classical $\Omega/\Phi$ scan ($D_x = 54$ mm, 0.3 deg/frame and 45 s for the exposure time). Satellite reflections are not observed anymore, and the cell parameters become $a_p\sqrt{2}$, $2a_p$, $a_p\sqrt{2}$, 90°, 90°, and 90°. The observed conditions limiting the possible reflections $0kl$, $k + l = 2n$; $hk0$, $h = 2n$; $h00$, $h = 2n$; $0k0$, $k = 2n$; and $00l$, $l = 2n$ are consistent with the space group *Pnma*. These crystal data are also gathered in Table 1.

The cell parameters obtained for the ordered state (that is, 150 K and rt) are very close; they are characteristic of an O′-type distortion ($a/2 > c > b/\sqrt{2}$), usually associated in manganites with a cooperative Jahn−Teller effect. In the disordered state (i.e., 373 K), the lattice exhibits an O-type distortion ($a > b/\sqrt{2} > c$), due to the increase of the $b$ parameter associated with the decrease of the others.

(24) Petricek, V.; Dusek, M. *Jana2000−The Crystallographic Computing System*; Institute of Physics: Praha, Czech Republic, 2000. The program can be obtained from http://sdpd.univ-lemans.fr/DU-SDPD/nexus/jana-sds/jana/jana.htm.

## Structure Determination

The interest of a superspace approach is not immediately obvious for short-period commensurate structures, but it does provide a general way to unify the description of series where the modulation evolves from commensurate to incommensurate, depending on the temperature or on the composition. Moreover, it allows analysis the different possible space groups of the supercell ($Pnm2_1$, $P12_1/m1$, and $P1m1$) just by changing the origin of the section of the supercrystal, as detailed below. This last point is particularly interesting in our case since three different space groups can be considered to model the superstructure of the $Bi_{1-x}Ca_xMnO_3$ series.

Using only the main reflections, the average structure in the cell $a_p\sqrt{2}, 2a_p, a_p\sqrt{2}, 90°, 90°, 90°$ has been solved at rt as well as at 150 K, allowing the localization of all the atoms. To evidence the existence of possible twinned domains, the twin laws referring to the pseudocubic nature of these perovskite-type structures were introduced in the refinement procedure for the two crystals $Bi_{0.6}Ca_{0.4}MnO_3$ and $Bi_{0.55}Ca_{0.45}$-$MnO_3$. The ratios of the six twinning variants have been refined. The main domain represents about 99% of the crystal volume, confirming the quasi-single-domain character of the crystals and, by the way, their high quality for X-ray refinement. The two $Bi_{0.6}Ca_{0.4}MnO_3$ and $Bi_{0.55}Ca_{0.45}MnO_3$ single crystals selected for the X-ray diffraction study were crushed and characterized by transmission electron microscopy. The electron diffraction investigation confirmed the rareness of twinning domains, and the bright/dark-field imaging study showed that they only appear in the form of very small twinned areas corresponding to two variants generated by the permutation of $\vec{a}$ and $\vec{c}$, on one hand, and of $\vec{b}$ and [101], on the other hand. The presence of oriented domains often hinders accurate refinement of the distorted perovskite-type manganites; the weak amount of observed twinned domains in our samples prevents such effects.

Thereafter, to simplify the description of the refinement procedure, only $Bi_{0.6}Ca_{0.4}MnO_3$ will be considered; it could be generalized for $Bi_{0.55}Ca_{0.45}MnO_3$.

Using only satellite reflections, a starting superspace model is determined by applying small displacements along $x$, $y$, and $z$ to the different atoms. Each atom is thus described with an average position $r_0$ and a displacement $U$; this displacement is expanded using a Fourier series:

$$U(\bar{x}_4) = \sum_n A_n \sin 2n\pi\bar{x}_4 + B_n \cos 2\pi\bar{x}_4 \qquad (1)$$

The sign of these displacements is tested via a trial and error method. All the reflections can then be used; a unitary weighting scheme is considered to increase the weight of the satellite reflections in the refinement and then to improve the convergence. The harmonics used to describe the displacements of all the atoms have been developed up to first order ($n = 1$ in eq 1).

To take into account the partial occupancy of the Bi site by Ca species, a modulation of substitution has been introduced. The average occupancy of the site corresponds to 0.60(1) Bi/0.40(1) Ca. The modulation function, intro-

**Table 2. $Bi_{0.6}Ca_{0.4}MnO_3$ Average (av), Displacement ($A_1$ and $B_1$, Fourier Terms from Eq 1), and Isotropic Thermal Motion Parameters Refined in the 4D Approach at 150 K**

| atom | harmonic | $x$ | $y$ | $z$ | $U_{eq}$ (Å) |
|---|---|---|---|---|---|
| Bi/Ca | av | −0.54609(10) | 0.25§ | 0.49153(9) | 0.00486(17) |
| | $A_1$ | 0.00245(18) | $0^b$ | −0.01835(15) | |
| | $B_1$ | $0^a$ | $0^b$ | 0.00329(13) | |
| | occupancy | | | | |
| | av | 0.580(11)/0.420(11) | | | |
| | $A_1$ | −0.029(3)/0.029(3) | | | |
| | $B_1$ | −0.013(3)/0.013(3) | | | |
| Mn(1) | av | $0^b$ | $0.5^b$ | $0.5^b$ | 0.0016(4) |
| | $A_1$ | −0.0020(4) | −0.0021(3) | 0.0196(3) | |
| | $B_1$ | $0^b$ | $0^b$ | $0^b$ | |
| O(1) | av | 0.0203(12) | $0.25^b$ | 0.5804(13) | 0.0061(14) |
| | $A_1$ | 0.0061(15) | $0^b$ | 0.0201(17) | |
| | $B_1$ | 0.0089(17) | $0^b$ | $0^a$ | |
| O(2) | av | 0.2876(8) | 0.5416(7) | 0.7087(9) | 0.0065(11) |
| | $A_1$ | $0^a$ | 0.0009(8) | −0.0056(12) | |
| | $B_1$ | −0.0030(11) | 0.0016(10) | −0.0359(14) | |

[a] Fixed because not significant. [b] Fixed by symmetry.

duced for describing the Bi/Ca distribution, is not significant, outlining a random Bi/Ca distribution on the site.

Crystallographic analysis based on the superspace formalism provides the structure of a supercrystal in a space of higher dimension; the actual structure of the crystal corresponds to a section of the supercrystal by the physical space. In the supercrystal atoms are described using atomic strings running along the $x_4$ axis. For an incommensurate phase, due to the irrational value of the $\mathbf{q}^*$ wave vector, all the points of the atomic strings can be reached and then all the choices of origin $t_0$ along $x_4$ for the section are relevant. For a commensurate phase, only some points of the atomic strings have a physical meaning and then the choice of this origin $t_0$ becomes crucial. All the possible sections as well as their symmetries should be identified. A symmetry operator changing the $\mathbf{q}^*$ vector into $-\mathbf{q}^*$ would belong to all the sections, while the symmetry operators leaving $\mathbf{q}^*$ invariant are present only in some particular sections. Thus, in the present case, the particular $t_0 = 0$ and $t_0 = 1/8$ sections have been identified; they correspond to the 3D symmetries $P12_1/m1$ and $Pnm2_1$, respectively. For any other section of the supercrystal, the corresponding 3D space group is $P1m1$. All these sections of the supercrystal have been tested. For $Bi_{0.6}$-$Ca_{0.4}MnO_3$, the section $t_0 = 0$ leads to an agreement factor of 19.5% on the satellite reflections against 11.8% in the section $t_0 = 1/8$, showing that the $P12_1/m1$ space group cannot allow a good modeling of the structure. Therefore, the section $t_0 = 1/8$ was considered afterwards. As expected for such a transverse modulation, the main displacement direction of all the atoms is observed along the $\vec{c}$ axis. The main results of this refinement are given in Table 2. At this stage of the refinement, the atomic displacements are modeled using harmonic functions (Fourier series developed up to the first order). Real displacements are certainly more complex, and then such a 4D treatment is oversimplified. To relax the resulting restraints, the superstructure (cell $2a_p\sqrt{2}, 2a_p, a_p\sqrt{2}, 90°, 90°, 90°$) was extracted and refined in a classical 3D way. This procedure has been applied for the data collected at 150 and 300 K. The model is then refined, and it quickly converges. The atomic positions in the $Pnm2_1$ supercell, obtained for $Bi_{0.6}Ca_{0.4}MnO_3$ at 150 K, are reported in Table 3a. Different refinements in the $P1m1$

**Table 3. Atomic Coordinates and Thermal Parameters at 150 K in the Supercell**

| atom | site | $x$ | $y$ | $z$ | occupation | $U_{iso}$ (Å$^2$) |
|---|---|---|---|---|---|---|
| | | | (a) $Bi_{0.6}Ca_{0.4}MnO_3$ | | | |
| Bi/Ca(1) | 2a | 0.85084(9) | 0.5$^a$ | 0.5 | 0.62(2)/0.38(2) | 0.0055(3) |
| Bi/Ca(2) | 2a | 0.35192(10) | 0.5$^a$ | 0.4679(4) | 0.58(2)/0.42(2) | 0.0058(3) |
| Bi/Ca(3) | 2a | 0.39751(11) | 0.0$^a$ | 0.4932(3) | 0.58(2)/0.42(2) | 0.0039(2) |
| Bi/Ca(4) | 2a | 0.89721(10) | 0.0$^a$ | 0.5085(4) | 0.60(2)/0.40(2) | 0.0076(3) |
| Mn(1) | 4b | 0.12493(18) | 0.7489(3) | 0.5067(6) | 1$^b$ | 0.0023(4) |
| Mn(2) | 4b | 0.62623(19) | 0.7521(3) | 0.4799(5) | 1$^b$ | 0.0015(4) |
| O(1) | 2a | 0.8614(14) | 0.0$^a$ | 0.085(3) | 1$^b$ | 0.007(2) |
| O(2) | 2a | 0.1154(12) | 0.0$^a$ | 0.431(3) | 1$^b$ | 0.0019(17) |
| O(3) | 2a | 0.6159(14) | 0.0$^a$ | 0.399(3) | 1$^b$ | 0.006(2) |
| O(4) | 2a | 0.3674(16) | 0.0$^a$ | 0.059(4) | 1$^b$ | 0.011(3) |
| O(5) | 4b | 0.2334(13) | 0.711(2) | 0.196(3) | 1$^b$ | 0.015(2) |
| O(6) | 4b | 0.9809(8) | 0.7106(13) | 0.3179(19) | 1$^b$ | 0.0029(12) |
| O(7) | 4b | 0.4789(7) | 0.7086(13) | 0.2487(16) | 1$^b$ | 0.0007(11) |
| O(8) | 4b | 0.7314(8) | 0.7062(13) | 0.1951(17) | 1$^b$ | 0.0026(12) |
| | | | (b) $Bi_{0.55}Ca_{0.45}MnO_3$ | | | |
| Bi/Ca(1) | 2a | 0.85065(9) | 0.5$^a$ | 0.5$^a$ | 0.54(2)/0.46(2) | 0.0058(2) |
| Bi/Ca(2) | 2a | 0.35272(9) | 0.5$^a$ | 0.4695(3) | 0.52(2)/0.48(2) | 0.0071(3) |
| Bi/Ca(3) | 2a | 0.39565(10) | 0$^a$ | 0.49646(18) | 0.52 (2)/0.48(2) | 0.0059(2) |
| Bi/Ca(4) | 2a | 0.89685(11) | 0$^a$ | 0.5120(3) | 0.54(2)/0.46(2) | 0.0106(3) |
| Mn(1) | 4b | 0.12319(19) | 0.7469(2) | 0.5067(4) | 1$^b$ | 0.0062(3) |
| Mn(2) | 4b | 0.62630(17) | 0.7508(2) | 0.4811(4) | 1$^b$ | 0.0020(3) |
| O(1) | 2a | 0.8628(12) | 0$^a$ | 0.103(3) | 1$^b$ | 0.011(2) |
| O(2) | 2a | 0.1116(10) | 0$^a$ | 0.441(2) | 1$^b$ | 0.0029(14) |
| O(3) | 2a | 0.6162(12) | 0$^a$ | 0.417(2) | 1$^b$ | 0.0076(19) |
| O(4) | 2a | 0.3717(13) | 0$^a$ | 0.074(3) | 1$^b$ | 0.013(2) |
| O(5) | 4b | 0.2335(11) | 0.7099(16) | 0.207(2) | 1$^b$ | 0.026(2) |
| O(6) | 4b | 0.9819(7) | 0.7101(11) | 0.3207(16) | 1$^b$ | 0.0078(13) |
| O(7) | 4b | 0.4790(6) | 0.7073(9) | 0.2554(12) | 1$^b$ | 0.0008(9) |
| O(8) | 4b | 0.7320(9) | 0.7067(12) | 0.2052(16) | 1$^b$ | 0.0114(15) |

$^a$ Fixed by symmetry. $^b$ Parameters fixed during the refinement.

space group, starting from different initial atomic positions, deduced from the $P12_1/m1$ and $Pnm2_1$ space groups, were carried out. All these refinements converge toward the model previously obtained in the $Pnm2_1$ space group; no significant deviation is observed. Moreover, despite the increasing number of refined parameters, the reliability factors are not improved. Then a lowering of symmetry from $Pnm2_1$ to $P1m1$ cannot be proved on the basis of the XRD refinements.

Finally, a refinement has been performed to determine the orthorhombic structure (*Pnma*) of $Bi_{0.6}Ca_{0.4}MnO_3$ at high temperature (373 K).

## Accurate Symmetry Analysis

In the previous section, it is clearly shown that the "$Pnm2_1$ model" allows a better fit of our data than the "$P2_1/m$ model". However, a tiny as previously reported for $Pr_{0.6}Ca_{0.4}MnO_3$,[11] cell distortion ($\beta = 90.76(2)°$) and possible lowering of symmetry leading to the $P1m1$ space group could be considered (cell $2a_p\sqrt{2}, 2a_p, a_p\sqrt{2}, 90°, \beta, 90°$). An accurate analysis of the symmetry has thus been performed by combining SHRPD and electron diffraction (ED) at low temperature.

The X-ray powder diffraction experiment was performed at ESRF (Grenoble, France) on the ID31 beam line. Several crystals picked from the batch of that used for XRD were crushed to obtain 30 mg of powder. Data were collected at 373 K, rt, and 150 K using a wavelength of 0.4 Å. Figure 2a shows a focus on the experimental peak observed for $2\theta$ close to 11.9° at 150 K; it can be associated with the 402 and $\bar{4}02$ reflections in the supercell description (cell $2a_p\sqrt{2}$, $2a_p, a_p\sqrt{2}, 90°, 90°, 90°$). These two reflections are equivalent in the orthorhombic symmetry, but a splitting of

the peak should be observed in the monoclinic one, as evidenced for $Pr_{0.6}Ca_{0.4}MnO_3$.[11] Figure 2b shows a simulation of the 402 and $\bar{4}02$ reflections using a monoclinic hypothesis ($\beta = 90.05°$) and the profile parameters of the ID31 diffractometer. Despite the tiny deviations expected for $\beta$ ($\beta = 90° + \epsilon$), the experimental resolution should allow the observation of such a small splitting up to $\epsilon = 0.025°$. Comparing parts a and b of Figure 2 confirms the absence of a $\beta$ deviation with regard to 90° for $Bi_{0.6}Ca_{0.4}MnO_3$. This ESRF study allows confirmation of the orthorhombic metric of the system.

The reconstruction of the reciprocal space was carried out at 90 K using a JEOL 2010 electron microscope. For the different crystal flakes, the selected area in the ED working mode was varied, using different apertures for recording the whole crystallite or selecting small zones and testing the homogeneity of the crystal. Three characteristic ED patterns, [010], [100], and [001], are given in parts a, b, and c, respectively, of Figure 3, where they are compared to the theoretical ones calculated using the atomic positions refined in the $Pnm2_1$ space group (Table 3a). The large majority of the experimental [100] ED patterns exhibit the condition limiting possible reflections $0kl$, $k + l = 2n$, confirming the existence of an $n$ glide mirror in agreement with the $Pnm2_1$ space groups for the $a \approx 2a_p\sqrt{2}$, $b \approx 2a_p$, $c \approx a_p\sqrt{2}$ supercell. When working with small apertures, very weak extra reflections $0kl$, $k + l = 2n + 1$, can be observed in some [100] SAED (small-area electron diffraction) patterns, suggesting local structural distortion, which could be generated by different effects such as the oxygen content, the Bi/Ca distribution, and also the role of the $6s^2$ lone pair of $Bi^{3+}$. Nevertheless, this local distortion is both very weak and rarely observed. Moreover, the bright/dark-field imaging study confirmed the absence of microtwinning phenomena and tweedlike contrasts, which are commonly associated with such small monoclinic distortion in manganites.[25] This electron microscopy study is then in agreement with all our XRD experiments.

SHRPD and ED investigations are both in agreement with the orthorhombic metric (in the limit of accuracy of the techniques, i.e., $\beta = 90°$ with $\Delta\beta < 0.02°$). They validate the choice of the $Pnm2_1$ space group for the refinement of the $Bi_{0.6}Ca_{0.4}MnO_3$ superstructure.

## Temperature Dependence of the Structures

**Analysis of the *Pnma* Structure at $T = 373$ K.** At high temperature, i.e., above $T_{co}$, a single Mn site is used for describing the structure in the *Pnma* space group. Two apical Mn−O(1) distances equal to 1.959(2) Å and four equatorial Mn−O(2) distances equal to 1.977(6) Å are observed. The resulting Mn environment corresponds thus to a quite regular octahedron (slightly flattened), and the angle Mn−O(2)−Mn ≈ 154° evidences the octahedron tilt in the polyhedral framework. This structure provides us with a reference for the geometry of one $MnO_6$ octahedron unaffected by CO/OO distortion, useful for analyzing low-temperature results.

(25) van Tendeloo, G.; Lebedev, O. I.; Hervieu, M.; Raveau, B. *Rep. Prog. Phys.* **2004**, *1315*, 67.
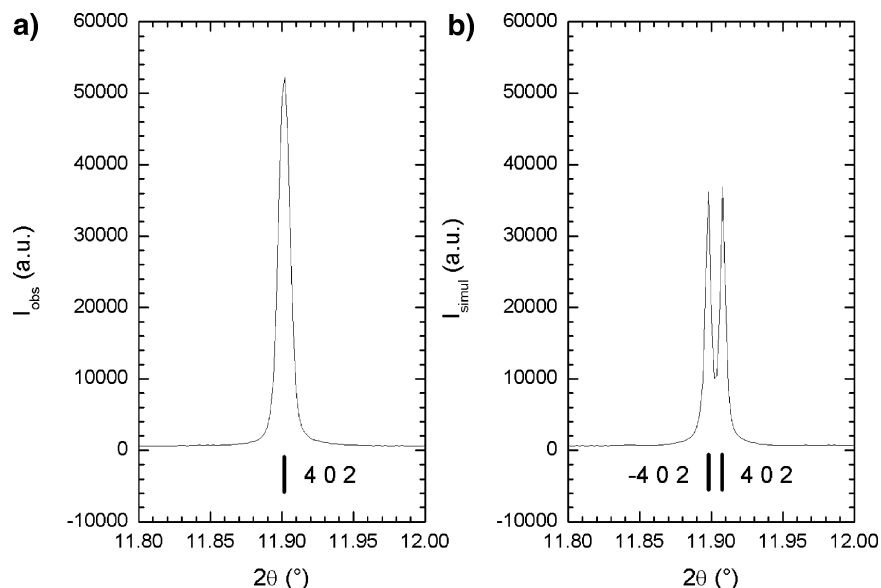
**Figure 2.** High-resolution synchrotron diffraction patterns. Focus on the position of the 402 reflection: (a) observed and (b) simulated in monoclinic symmetry with $\beta = 90.05°$. The indices are those of the $Pnm2_1$ supercell.

**Analysis of the $Pnm2_1$ Structure at $T = 150$ K.** The projection of the structure of $Bi_{0.6}Ca_{0.4}MnO_3$ along $\vec{b}$ and the calculated interatomic distances obtained from the data at 150 K are given in Figure 4. One observes two sites for manganese, labeled Mn(1) and Mn(2), whose average Mn—O distances are close, i.e., $\langle Mn(1)-O\rangle = 1.98(3)$ Å and $\langle Mn(2)-O\rangle = 1.96(3)$ Å. Bearing in mind the significantly larger size of $Mn^{3+}$ (0.64 Å) compared to $Mn^{4+}$ (0.53 Å) according to Shannon,[26] this similarity suggests the absence of formal charge ($Mn^{3+}$ and $Mn^{4+}$) ordering in this oxide. This is also in agreement with the bond valence sum calculations,[27] which lead to 3.42 and 3.55 for Mn(1) and Mn(2). However, the comparison of the Mn—O distances (Table 5) in the basal plane of the high-temperature and 150 K structures outlines the distortion of the octahedra.

The $Mn(1)O_6$ octahedra are clearly elongated in the basal plane, with two opposite long Mn—O equatorial distances (2.08(2) and 2.07(1) Å), two short equatorial distances (1.90(1) and 1.91(1) Å), and two medium apical distances (1.94(1) and 1.95(1) Å). The direction of the longer Mn—O equatorial distances corresponds to the orientation of the $d_{z^2}$ orbitals. Consequently, the elongation of this $Mn(1)O_6$ octahedron resembles a "small" Jahn—Teller distortion; they can be compared, as examples, to those observed at rt in $LaMnO_3$ (two long Mn—O equatorial distances, 2.178(1) Å, two short Mn—O equatorial distances, 1.907(1) Å, and two medium apical distances, 1.9680(3) Å[28]) and in $BiMnO_3$ (two long Mn—O equatorial distances, 2.2 Å, two short Mn—O equatorial distances, 1.8 Å, and two medium apical distances, 2.0 Å[29]).

The description of the $Mn(2)O_6$ octahedron is more ambiguous; the basal plane of the octahedron is less distorted. Two intermediate Mn(2)—O distances (1.95(3) and 1.96(1) Å), 90° oriented, are observed, and the two others, also 90°

oriented, are shorter (1.88(1) Å) and longer (2.07(1) Å). It still results in an elongation of the octahedron, which is however less pronounced than that of $Mn(1)O_6$. The longer diagonals O(5)—Mn(2)—O(7) are evidenced in Figure 4. Two descriptions of the structure can be proposed.

In the first description, the $Mn(1)O_6$ and $Mn(2)O_6$ octahedra form double layers $[Mn(1)/Mn(1)]_\infty$ and $[Mn(2)/Mn(2)]_\infty$, parallel to (100) and alternating along $\vec{a}$ (Figure 4, left part).

In the second description, one considers that the structure is built up from double ribbons of $Mn(1)/Mn(2)]_\infty$ (Figure 4, right part). The elongated diagonals of the octahedron within "Mn(1)/Mn(2)" pairs, i.e., $d_{z^2}$ orbitals, are almost collinear, with Mn(1)—O(5)—Mn(2) angles of 156°. Thus, the structure of $Bi_{0.6}Ca_{0.4}MnO_3$ is strongly governed by a fish-bone-type ordering of the $d_{z^2}$ orbitals of manganese based on the existence of Mn(1)/Mn(2) pairs characterized by an orbital overlapping. These atomic pairs have been associated with Zener polarons in ref 11.

The right part of Figure 4 shows the distribution of the different oxygens in the basal plane; the role of O(7) and O(6), which connect two adjacent [Mn(1)/Mn(2)] pairs of octahedra, will be detailed in the analysis of HREM images.

**Analysis of the Structure at $T = $ rt: Average Effect?** At rt, due to the width of the CO/OO transition and the proximity of the data collection temperature from $T_{CO}$, the transition could be considered to be still evolving. As mentioned above, the extra reflections in the ED patterns, which are the signatures of the ordering, are clearly visible at room temperature for numerous crystallites. The room temperature structure of $Bi_{0.6}Ca_{0.4}MnO_3$ is considered as also characterized by a doubling of the $a$ parameter and the same symmetry as the low-temperature one, i.e., an orthorhombic cell with $2a_p\sqrt{2}$, $2a_p$, and $a_p\sqrt{2}$ and the space group $Pnm2_1$. However, for some crystallites, even working as further described with a low electron beam intensity and quickly recording the ED patterns, satellite reflections are not observed. The as-observed state could be thus associated with

(26) Shannon, R. D. *Acta Crystallogr., A* **1976**, *32*, 751−767.
(27) Brown, I. D. *J. Appl. Crystallogr.* **1996**, *29*, 479−480.
(28) Brown, D. *Acta Crystallogr., B* **1992**, *48*, 553−572.
(29) Brown, D.; Altermatt, D. *Acta Crystallogr., B* **1985**, *41*, 244−247.
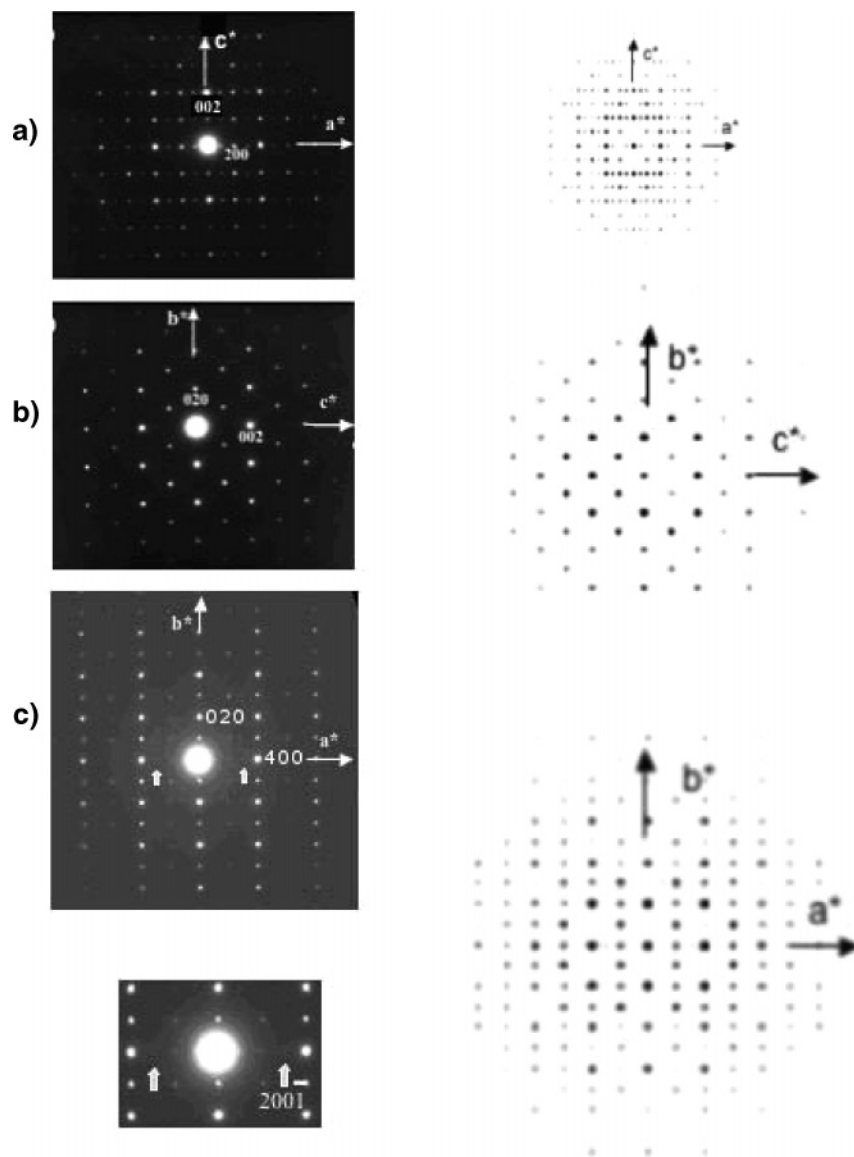
**Figure 3.** (a) [010], (b) [100], and (c) [001] ED patterns, recorded at 92 K, indexes in the *Pnm*2$_1$ supercell. The condition 0*kl*, *k* + *l* = 2*n* (b), confirms the existence of an *n* glide mirror. The *hk*0 extra reflections of the ordered phase are more intense for *h* = 2*n* than for *h* = 2*n*+ 1 (outlined by small white arrows in (c)). This is more easily visible in the enlarged pattern; the 003 reflection (denoted also as 200$\overline{1}$ in the 4D formalism, using *hklm* indices). The patterns on the right-hand side correspond to ED calculated from the refined *Pnm*2$_1$ model.

an intermediate state between the nonordered (with the high-temperature structure) and ordered (with the low-temperature structure) ones, and it outlines that the coexistence of two domains induces an average rt structure. This is in agreement with the SHRPD measurements, which evidence only one set of cell parameters at 373 K (>$T_{CO}$) and at 150 K (≪$T_{CO}$) but two sets of cell parameters at rt (slightly <$T_{CO}$).

The XRD data on the single crystal have been refined at rt. The oxygen environments of Mn(1) and Mn(2) are quite similar; two short (1.82(1) Å ≤ *d* ≤ 1.95(1) Å) and two long (2.07(2) Å ≤ *d* ≤ 2.08(1) Å) Mn–O distances are identified in the basal plane for each Mn (Figure 5), but d$_{z^2}$ orbitals cannot be evidenced by long diagonals as at 150 K. Accounting for the SHRPD and electron microscopy results, the interatomic distances and bond angles calculated on the basis of the refined model are no longer discussed herein. However, this result is interesting because it underlines the sensitivity of single-crystal X-ray diffraction to small atomic

displacements and justifies its use to explore such CO/OO transitions.

**Temperature Dependence of the Lattice Parameters.** Crushing crystals to record X-ray powder diffraction patterns complements this X-ray single-crystal analysis. The temperature-dependent structural characterization over the range 150−700 K was realized using the X-ray powder diffractometer Bruker D8 (Cu Kα, energy-dispersive SOL-X detector) equipped with an MRI TC-wide-range temperature chamber. The measurements were performed under an ambient atmosphere. Two scans were measured for each temperature and the measured intensities compared to check the thermal stabilization of the sample structure. The X-ray diffraction patterns were evaluated by Rietveld profile analysis using the FullProf_Suite of programs.[30] No spectacular structural transition is observed in this temperature

(30) Rodriguez-Carvajal, J.; Hennion, M.; Moussa, F.; Moudden, A. H.; Pinsard, L.; Revcolevschi, A. *Phys. Rev. B* **1998**, *57* (6), R3189.

**Figure 4.** Drawing of the 150 K structure of $Bi_{0.6}Ca_{0.4}MnO_3$, projected in the *ac* plane. In the left part, the light gray and dark gray polyhedra correspond to $Mn(1)O_6$ and $Mn(2)O_6$ ribbons, respectively. In the middle part, the in-plane interatomic distances are reported, while in the right part, the $d_{z^2}$ orbital order is modeled. Mn(1) and Mn(2) are symbolized using light gray and dark gray circles of medium size, respectively; oxygen atoms are represented by small circles and Bi/Ca atoms by large circles.

**Table 4. $Bi_{0.6}Ca_{0.4}MnO_3$ Atomic Positions and Isotropic Thermal Parameters at $T = 373$ K**

| name | site | $x$ | $y$ | $z$ | occupation | $U_{iso}$ (Å) |
|------|------|-----|-----|-----|-----------|---------------|
| Bi/Ca | 4c | 0.04345(15) | $0.25^a$ | 0.99448(14) | 0.58(2)/0.42(2) | 0.0126(3) |
| Mn | 4b | $0.5^a$ | $0.5^a$ | $0.0^a$ | $1^b$ | 0.0068(8) |
| O1 | 4c | 0.4825(19) | $0.25^a$ | 0.0722(18) | $1^b$ | 0.015(3) |
| O2 | 8d | 0.2077(11) | 0.5402(9) | 0.2063(11) | $1^b$ | 0.0159(18) |

$^a$ Fixed by symmetry. $^b$ Parameters fixed during the refinement.

range. Consequently, due to the quality of the data and notably the weak intensity of the satellite reflections, all patterns were refined using the *Pnma* subcell ($a_p\sqrt{2}$, $2a_p$, $a_p\sqrt{2}$, 90°, 90°, 90°). These calculations lead to an interesting evolution, which is reported in Figure 6. As previously discussed, the low-temperature structure exhibits an O′-type distortion ($a > c > b/\sqrt{2}$), associated with a cooperative Jahn−Teller effect in the manganites. The three parameters increase slowly with the temperature, and a variation of the lattice parameters appears at $T \approx 310$ K. The structure becomes at that time an O type ($a > b/\sqrt{2} > c$); the transition occurs in a temperature range of ~20 K. This structural effect, associated with the orbital ordering phenomenon, is also visible in the volume vs $T$ curve given in the inset of Figure 6. The hysteresis effect has also been studied in the vicinity of the structural transition, from 180 to 360 K. This study shows a difference of ~10 K for the characteristic temperatures in increasing and decreasing modes; the transition temperature is of course higher in the increasing branch. These modifications in the cell parameters, which arise just around room temperature, are thought to be responsible for the fragility of the crystals, and thus for their small size, as mentioned in the experimental part. They also lead to an average structure for the state observed at rt in the previous section.

**ED and HREM Study at rt.** The high-resolution electron microscopy studies were carried out at room temperature, with a TOPCON 002B electron microscope, having a 1.7 Å point resolution ($V = 200$ kV and $C_s = 0.4$ mm).

Keeping in mind the previous results, it is important to note that the [010] ED patterns and [010] images have been

recorded at rt. It should be noted that the extra reflections of a few crystallites are scarcely detectable or absent. Nevertheless, the HREM images recorded in the latter conditions are of interest since they are characteristic of the *Pnma*-type structure, and the experimental homogeneous contrasts of the through-focus series attest to the random distribution of the Bi and Ca atoms in the crystallites, in agreement with X-ray diffraction results. For the majority of the crystallites, the intensity of the satellites and the specific contrasts of certain HREM images associated with the CO/OO effect are clearly visible at rt. However, after a long exposure time under an intense electron beam (typically, 10 min or a few tens of minutes, which are common conditions for HREM observations), they could decrease, so we worked using a low electron beam intensity and shortening the observation times for avoiding transition phenomena. Theoretical images have been calculated for the ordered structures, using the refined parameters in Table 3 and varying the crystal thickness in the range 23−100 Å and the focus values. They allow correlation of the observed images with the refined structural characteristics.

The experimental through-focus series shows that $2a_p\sqrt{2}$ and the periodicity, which are the signatures of CO/OO, are visible for certain focus values. Two of these characteristic contrasts are given in Figure 7. In the top part of each panel, the simulated images are inset into the experimental images, whereas in the bottom part of each panel, a small zone is exaggeratedly enlarged to be compared with the [010] projections of the structure, by considering the octahedron framework with gray $Mn(1)O_6$ octahedra and dark $Mn(2)O_6$ octahedra.

The first signature, obtained for focus values where the high electron density areas are imaged as brighter dots, is the "double-band" contrast. This effect is only observed in the thicker parts of the crystallites (estimated between 60 and 100 Å), in the form of two adjacent rows of gray spots alternating with two adjacent rows of less gray spots. The calculated images ($t = 90$ Å and $\Delta f \approx -900$ Å for the inset

**Table 5. Cation−Oxygen Distances (Å) at 150 K[a]**

| Bi(1)−O(1)[i] | 3.191(16) | Bi(2)−O(1)[iii] | 2.424(16) | Bi(3)−O(2) | 3.114(13) | Bi(4)−O(1) | 2.325(18) |
|---|---|---|---|---|---|---|---|
| Bi(1)−O(2)[ii] | 3.101(15) | Bi(2)−O(3)[ii] | 3.099(18) | Bi(3)−O(3) | 2.450(16) | Bi(4)−O(1)[ix] | 3.144(18) |
| Bi(1)−O(2)[iii] | 2.361(15) | Bi(2)−O(3)[iii] | 2.358(18) | Bi(3)−O(4) | 2.37(2) | Bi(4)−O(2)[xi] | 2.430(13) |
| Bi(1)−O(4)[iii] | 2.415(18) | Bi(2)−O(4)[iii] | 3.119(18) | Bi(3)−O(4)[ix] | 3.08(2) | Bi(4)−O(3) | 3.143(16) |
| Bi(1)−O(5)[iv] | 2.600(15) | Bi(2)−O(5) | 2.535(15) | Bi(3)−O(5)[x] | 3.259(15) | Bi(4)−O(5)[iii] | 2.376(15) |
| Bi(1)−O(5)[v] | 2.600(15) | Bi(2)−O(5)[vii] | 2.535(15) | Bi(3)−O(5)[vii] | 3.259(15) | Bi(4)−O(5)[v] | 2.376(15) |
| Bi(1)−O(6) | 2.356(10) | Bi(2)−O(7) | 2.418(9) | Bi(3)−O(7)[x] | 2.724(9) | Bi(4)−O(6)[x] | 2.592(10) |
| Bi(1)−O(6)[vi] | 3.343(10) | Bi(2)−O(7)[iv] | 3.260(9) | Bi(3)−O(7)[iii] | 2.500(9) | Bi(4)−O(6)[i] | 2.671(10) |
| Bi(1)−O(6)[vii] | 2.356(10) | Bi(2)−O(7)[vii] | 2.418(9) | Bi(3)−O(7)[vii] | 2.724(9) | Bi(4)−O(6)[vii] | 2.592(10) |
| Bi(1)−O(6)[viii] | 3.343(10) | Bi(2)−O(7)[v] | 3.260(9) | Bi(3)−O(7)[v] | 2.500(9) | Bi(4)−O(6)[viii] | 2.671(10) |
| Bi(1)−O(8) | 2.623(10) | Bi(2)−O(8)[iv] | 2.702(10) | Bi(3)−O(8)[iii] | 2.374(10) | Bi(4)−O(8)[x] | 3.338(10) |
| Bi(1)−O(8)[vii] | 2.623(10) | Bi(2)−O(8)[v] | 2.702(10) | Bi(3)−O(8)[v] | 2.374(10) | Bi(4)−O(8)[vii] | 3.338(10) |
| Mn(1)−O(1)[iii] | 1.939(5) | Mn(2)−O(3)[xii] | 1.932(5) | | | | |
| Mn(1)−O(2)[xii] | 1.949(4) | Mn(2)−O(4)[iii] | 1.959(5) | | | | |
| Mn(1)−O(5) | 2.080(15) | Mn(2)−O(5)[iv] | 1.953(15) | | | | |
| Mn(1)−O(6)[xiii] | 1.904(10) | Mn(2)−O(7) | 2.070(8) | | | | |
| Mn(1)−O(6)[iv] | 2.068(10) | Mn(2)−O(7)[iv] | 1.880(9) | | | | |
| Mn(1)−O(8)[iv] | 1.908(9) | Mn(2)−O(8) | 1.956(10) | | | | |

[a] Key: (i) 2 − x, 1/2 − y, 1/2 + z; (ii) 1 − x, 1/2 − y, −1/2 + z; (iii) 1 − x, 1/2 − y, 1/2 + z; (iv) 1 − x, 3/2 − y, 1/2 + z; (v) 1 − x, −1/2 + y, 1/2 + z; (vi) 2 − x, 3/2 − y, 1/2 + z; (vii) x,1 − y, z; (viii) 2 − x, −1/2 + y, 1/2 + z; (ix) x, y, 1 + z; (x) x, −1 + y, z; (xi) 1 + x, y, z; (xii) x,1 + y, z; (xiii) −1 + x, y, z.



**Figure 5.** Drawing of the rt structure of Bi$_{0.6}$Ca$_{0.4}$MnO$_3$, projected in the *ac* plane. In the left part, the light gray and dark gray polyhedra correspond to Mn(1)O$_6$ and Mn(2)O$_6$ ribbons, respectively. In the right part, the in-plane interatomic distances are reported.



**Figure 6.** Temperature dependence of the lattice parameters, from X-ray powder diffraction (*Pnma* space group: $a_p\sqrt{2}$, $2a_p$, $a_p\sqrt{2}$); the cell volume is also plotted in the inset.

one in Figure 7a) confirm that the double-band effect with double rows of gray and less gray spots is generated for crystal thicknesses higher than 60 Å, as experimentally observed. They confirm that all the bright spots are associated

with the cation positions: the double rows of gray spots are associated with the double rows of Mn(1), and Bi/Ca(1) and Bi/Ca(4), whereas the darker ones correspond to the double rows of Mn(2), and Bi/Ca(2) and Bi/Ca(3). From the calculated images, it appears that the tiny contrast difference between the two types of double rows (gray and less gray) is generated by the difference in the cation environments. Such image contrast is of interest since it shows that one important signature of the ordering is the existence of alternating cation double rows.

The second contrast (Figure 7b) is more easily visible and characterized, for focus values where the low electron density zones are highlighted, by the appearance of single brighter rows (see the vertical bright arrows in Figure 7b), spaced by 11 Å along $\vec{a}$. The origin of the single bright row, as observed in Figure 7b (t = 30 Å and $\Delta f \approx −225$ Å) is more difficult to interpret directly in terms of the projected structure. The rows of brighter spots are indeed associated with the positions of the oxygen O(6), which is the common vertex between the two Mn(1)O$_6$ octahedra in the equatorial plane (Figure 4). The positions of the oxygen O(7), which is the matching atom in the adjacent double band, i.e., the common vertex between the two Mn(2)O$_6$ octahedra in the equatorial plane, exhibit a darker contrast (top of Figure 7b). We have to keep in mind that the *Pnma* structure exhibits a single position for the equatorial oxygens which, through the ordering phenomena, turns into four different positions, O(5), O(6), O(7), and O(8). This peculiar image highlights the different "roles" played by O(6) and O(7), separating the two types of double rows of octahedra.

Note that, in a general way, the associated contrasts are similar but considerably lighter than those previously reported for the Bi$_{1-x}$Sr$_x$MnO$_3$ compounds[16] and that the quality of the image is lowered by the fact that we work at a temperature close to the transition and that several contrast effects are recorded in rather thick zones. To draw a definite conclusion on the symmetry of this ordered state, calculations based on the $P2_1/m$ model have also been carried out; none of these simulated images provide contrasts completely fitting with the characteristic experimental ones, whatever the focus and crystal thickness. The model of the alternating single
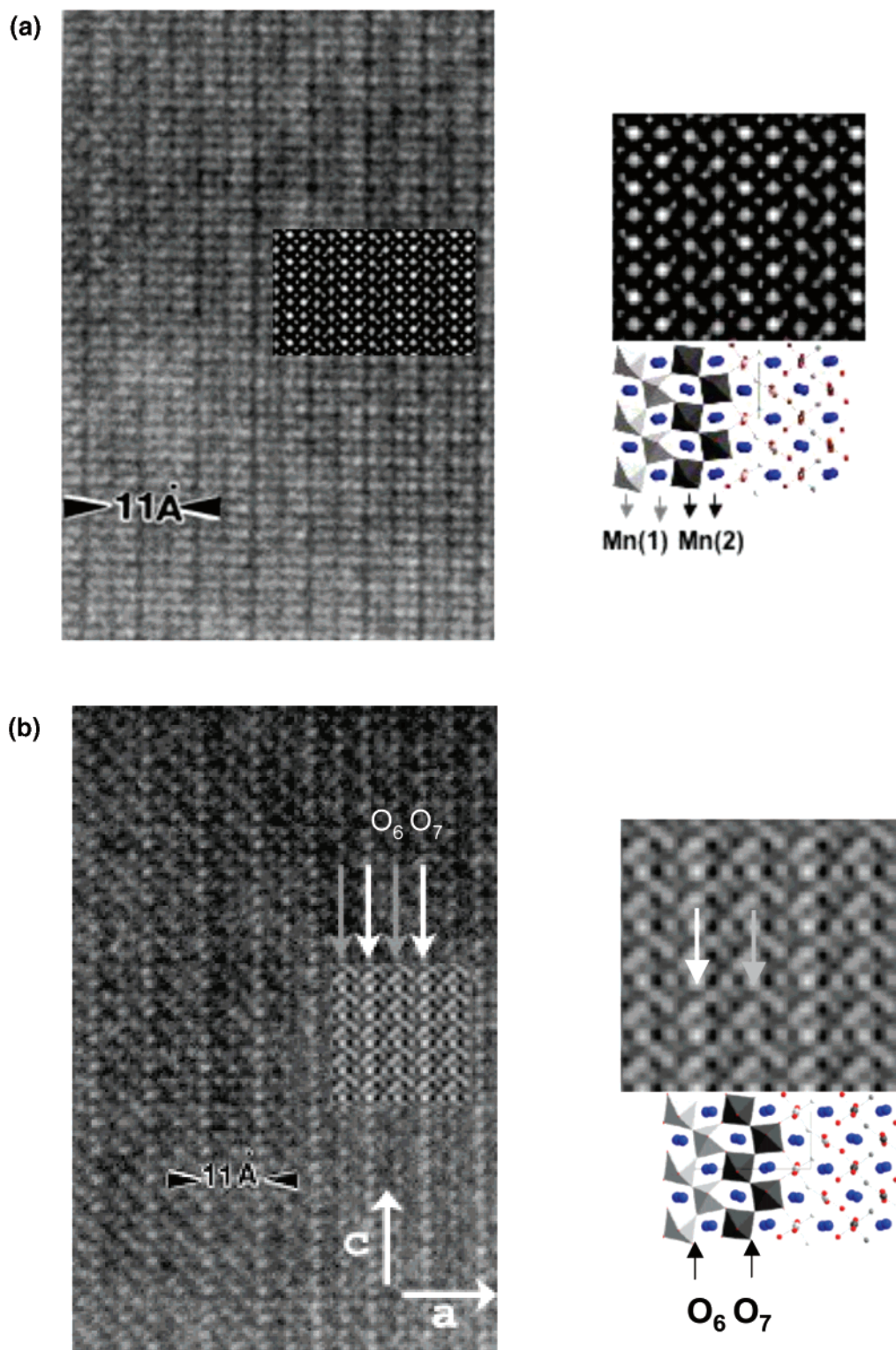
**Figure 7.** Examples of [010] HREM typical images, showing two signatures of the modulated structure. The simulated images are inset into the experimental ones. At the right of each panel, simulated image and structure are associated. (a) "Double-band" contrast, where the cation positions are highlighted. The double bands are associated with the double rows of $Mn(1)O_6$ and $Mn(2)O_6$ octahedra. (b) Example of an image showing 11 Å spaced rows of bright spots, associated with the positions of the O(6) oxygens. White and gray arrows are associated with O(6) and O(7) oxygen positions, respectively.

rows of "$Mn^{3+}$" and "$Mn^{4+}$" can then be definitively refuted for $Bi_{0.6}Ca_{0.4}MnO_3$.

**Comparison with $Bi_{0.55}Ca_{0.45}MnO_3$.** The two samples $Bi_{0.6}Ca_{0.4}MnO_3$ and $Bi_{0.55}Ca_{0.45}MnO_3$ are characterized by similar ED patterns, HREM images, and behavior under the electron beam. The same procedure has been followed to study a single crystal of this close composition. The different

refinements carried out lead to atomic coordinates and thermal parameters which are very close to those obtained for $Bi_{0.6}Ca_{0.4}MnO_3$. This is only illustrated by the 150 K results given in Table 3b. They lead to similar descriptions of the supercell and MnO framework, but the Mn−O distances between the two samples are not compared due to the lack of precision concerning the oxygen positions in the
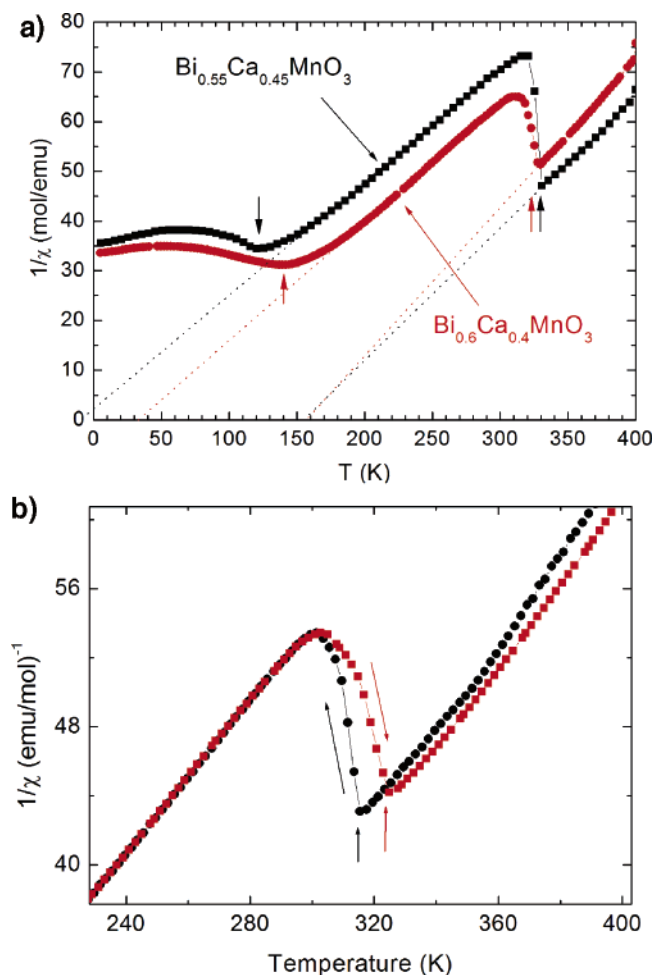
**Figure 8.** (a) Inverse susceptibility curve versus temperature of Bi$_{0.6}$Ca$_{0.4}$-MnO$_3$ and Bi$_{0.55}$Ca$_{0.45}$MnO$_3$ (1.4 T, zero-field cooling, temperature increasing). The vertical arrows indicate the characteristic temperatures ($T_N$ and $T_{CO}$). (b) Inverse susceptibility curves versus temperature of Bi$_{0.6}$Ca$_{0.4}$MnO$_3$. Grey and black symbols correspond to measurements performed increasing and decreasing $T$, respectively.

absence of neutron diffraction data (not yet performed, due to the too small size of the crystals).

## Magnetic Properties

The magnetic measurements were performed by using several crystals together for each compound to have 0.03 g in a SQUID magnetometer, at 1.4 T, increasing the temperature from 5 to 400 K.

The magnetization curves of both samples have similar shapes. They are characteristic of antiferromagnets with maximal moments reaching only $\cong 0.075$ $\mu_B$ at 1.4 T with a small field-cooled−zero-field-cooled effect. Only the inverse susceptibility versus $T$ curves are shown Figure 8. They allow two characteristic temperatures to be determined for each sample. The charge order temperatures are very close, slightly higher for Bi$_{0.55}$Ca$_{0.45}$MnO$_3$ ($T_{CO} \cong 330$ K) than Bi$_{0.6}$Ca$_{0.4}$-MnO$_3$ ($T_{CO} \cong 327$ K). In contrast the difference between the Neel temperatures ($T_N$) is more important and lower for Bi$_{0.55}$Ca$_{0.45}$MnO$_3$ ($T_N \cong 122$ K) than Bi$_{0.6}$Ca$_{0.4}$MnO$_3$ ($T_N \cong 140$ K). In the same way, the structural (at $T_{CO}$) and magnetic (at $T_N$) transitions are a little bit broader for Bi$_{0.6}$Ca$_{0.4}$MnO$_3$ than Bi$_{0.55}$Ca$_{0.45}$MnO$_3$. Note at this point that it should be very interesting to characterize crystals of Bi$_{0.5}$Ca$_{0.5}$MnO$_3$

to confirm (or not) this evolution and particularly to know if the domain between $T_{CO}$ and $T_N$ continues to increase. For each compound, two linear paramagnetic domains are evidenced above $T_{CO}$ and between $T_{CO}$ and $T_N$; they allow determination of two critical paramagnetic temperatures ($\Theta_p$). The highest $\Theta_p$ is similar for both compounds ($\Theta_{p,HT} \cong 160$ K), evidencing ferromagnetic correlations. The lowest $\Theta_p$ corresponds to the Debye temperature; it decreases from +30 K for Bi$_{0.6}$Ca$_{0.4}$MnO$_3$ to −10 K for Bi$_{0.55}$Ca$_{0.45}$MnO$_3$, indicating a reinforcement of the antiferromagnetic interactions when the Bi/Ca ratio decreases. It is difficult to fit the data by a Curie−Weiss law due to the short temperature range of the linear regions, particularly for the high-temperature domains. In fact, it should be interesting to extract the $\mu_{eff}$ value for each domain to compare them and test the validity of the Zener polaron proposed for Pr$_{0.6}$Ca$_{0.4}$-MnO$_3$.[11]

The bump (Figure 8b) attributed to the CO is moved to lower temperatures (from ∼10 K) when the measurement is made at decreasing temperature in agreement with the X-ray data.

Unfortunately, transport properties have not been studied due to the too small size ($V \leq 0.1 \times 0.1 \times 0.1$ mm$^3$) of the samples.

## Discussion and Concluding Remarks

The difficulty in obtaining one "ideal sample" (large crystals without twinning domains), the number of various intrinsic parameters in such ternary oxides, and the pseudo-symmetry of the structures make necessary the use of complementary techniques. The structures of Bi$_{1-x}$Ca$_x$MnO$_3$ with $x = 0.4$ and 0.45 have been solved using single-crystal X-ray diffraction at different temperatures, above, just below, and far below $T_{CO}$, HREM, in connection with X-ray powder diffraction, and magnetization measurements. The structure determination has been successfully performed thanks to the growth of the single-variant nature of the crystals.

The most important result deals with the determination of the space group of the ordered phase at 150 K, using the 4D formalism as the starting point, combined with information from SHRPD and TEM techniques. The study at 150 K leads to the *Pnm*2$_1$ space group, and the atomic positions show that orbital ordering is the driving force of the structural transition. The elongation of the MnO$_6$ octahedra in the basal plane is associated with d$_{z^2}$ orbital ordering and with small Jahn−Teller distortions, in agreement with the cooperative effect shown by the evolution of the cell parameters versus temperature. The distortion of the MnO$_6$ octahedra leads to the formation of manganese pairs exhibiting almost collinear d$_{z^2}$ orbitals.

The results of the structural refinement and double-band contrast of HREM images are notably consistent. They show that the structure is thus better described by a 2:2 manganese order−as proposed in Pr$_{0.6}$Ca$_{0.4}$MnO$_3$[11]−than by a 1:1 order. Note that the structure analysis shows that the average charges of the two different manganese types are very close in Bi$_{0.6}$Ca$_{0.4}$MnO$_3$ and Bi$_{0.55}$Ca$_{0.45}$MnO$_3$, in agreement with the structure proposed for Pr$_{0.6}$Ca$_{0.4}$MnO$_3$[11] and in contrast with the classical picture of the 1:1 model.

$Bi_{1−x}Ca_xMnO_3$ ($T_{CO} \cong 330$ K for $x = 0.45$ and 0.4) behave in the same manner as Ln-based manganites for the temperature dependence of their cell parameters, related to the cooperative Jahn−Teller effect, but exhibit a higher ordering transition temperature ($T_{CO} \cong 240$ K for $Pr_{0.6}Ca_{0.4}MnO_3$[11]). The strong antiferromagnetic character of the Bi-based compounds was previously outlined by the marked differences in the critical magnetic fields found to induce ferromagnetism in $Bi_{0.5}Ca_{0.5}MnO_3$ and $Ln_{0.5}Ca_{0.5}MnO_3$.[31] As previously observed in ref 32, the steric rules, characterized by the A-site size and the associated mismatch, established in the (Ln, A)$MnO_3$ system[33−35] cannot however be applied for the Bi series. The particular effect of bismuth may be due to the stereoactivity of its electronic lone pair. In fact, local spin density approximation pseudopotential calculations indicate that covalent bonding between the bismuth and oxygen in $BiMnO_3$ introduces additional orbital interactions compared with the rare-earth manganites, in which the interaction is essentially purely ionic.[36] These Bi-based perovskites behave as Ln-based manganites for the temperature dependence of their cell parameters, related to the cooperative Jahn−Teller effect, but exhibit a higher stability of the CO/OO (high values for both $T_{CO}$ and $\mu_0 H_c$) than the Ln-based manganites. This peculiar behavior justifies further investigations of other Bi-based perovskite manganites, especially for correlating the evolution of the double-band ordered structures with the different properties. Single-crystal neutron diffraction data have been collected, and their studies are in progress.

**Supporting Information Available:** CIF information for $Bi_{0.597}Ca_{0.403}MnO_3$. This material is available free of charge via the Internet at http://pubs.acs.org.

CM060222H

(31) Atou, T.; Chiba, H.; Ohoyama, K.; Yamaguchi, Y.; Syono, Y. *J. Solid State Chem.* **1999**, *145*, 639−642.

(32) Rodríguez-Carvajal, J. *Physica B* **1993**, *192*, 55. For a more recent version see: Rodríguez-Carvajal, J. *Recent Developments of the Program FULLPROF*; CPD Newsletter 26; International Union of Crystallography: Chester, England, December 2001; available at http://journals.iucr.org/iucr-top/comm/cpd/Newsletters. The program can be obtained from at ftp://ftp.cea.fr/pub/llb/divers/fullprof.2k.

(33) Kirste, A.; Goiran, M.; Respaud, M.; Vanaken, J.; Broto, J. M.; Rakoto, H.; von Ortenberg, M.; Frontera, C.; Garcia-Munoz, J. L. *Phys. Rev. B* **2003**, *67*, 134413.

(34) Beran, P.; Malo, S.; Martin, C.; Maignan, A.; Nevøiva, M.; Hervieu, M.; Raveau, B. *Solid State Sci.* **2002**, *4*, 917−921.

(35) Rodríguez-Martínez, L. M.; Attfield, J. P. *Phys. Rev. B* **1996**, *54*, R15622.

(36) Rodríguez-Martínez, L. M.; Attfield, J. P. *Phys. Rev. B* **2000**, *63*, 024424.

(37) Attfield, J. P. *Cryst. Eng.* **2002**, *5*, 427−438.

(38) Hill, N. A.; Rabe, K. M. *Phys. Rev. B* **1999**, *59* (13), 8759.